Drug Design, Development and Therapy Dovepress

Open Access Full Text Article ORIGINAL RESEARCH

Protective Effect of Modified Suanmei-Tang on Metabolic-Associated Fatty Liver Disease: An Integrated Strategy of Network Pharmacology, Metabolomics, and Transcriptomics

Chao Wang[1,*], Mei Zhao[2,*], Yuanyuan Yue[3], Chao Hu[2], Chunqiu Zhou[2], Zhongyi Zhang[2], Yunliang He[4], Yaqi Luo[4], Tao Shen[2], Sijie Dang[4], Yang Yang[4], Yong Zhang[2,4]

[1]Traditional Chinese Medicine Department, Qitai Hospital of the Sixth Division, Xinjiang, 831899, People's Republic of China; [2]College of Basic Medicine, Chengdu University of Traditional Chinese Medicine, Chengdu, 611137, People's Republic of China; [3]Department of Ultrasound, Chengdu First People's Hospital, Chengdu, 610095, People's Republic of China; [4]Institute of Traditional Chinese Medicine, Sichuan Academy of Chinese Medicine Sciences, Chengdu, 610014, People's Republic of China

*These authors contributed equally to this work

Correspondence: Yong Zhang; Yang Yang, Institute of Traditional Chinese Medicine, Sichuan Academy of Chinese Medicine Sciences, Chengdu, People's Republic of China, Email 18692213920@163.com; 18721326@qq.com

Background: Modified Suanmei-Tang (MST) comprises four plants common to both traditional Chinese medicine and culinary applications, and it can potentially alleviate metabolic-associated fatty liver disease (MAFLD) triggered by a high-fat diet (HFD).

Purpose: This research aims to investigate the impact and underlying mechanisms of MST in ameliorating MAFLD caused by an HFD.

Methods: UHPLC-Q-Orbitrap-MS/MS was used to determine the constituents of MST and to evaluate its effects on MAFLD mouse models. Transcriptomics, network pharmacology, and bioinformatics analysis (including Kyoto Encyclopedia of Genes and Genomes and Gene Set Enrichment Analysis) were utilized to further clarify the mechanisms by which MST acts on MAFLD. The experimental methods included ELISA, real time quantitative PCR (RT-qPCR), Western blot, immunohistochemistry, molecular docking, and metabolomics. Transcriptomics was integrated with metabolomics to find correlations between differentially expressed genes and metabolites, and crucial genes were validated through RT-qPCR.

Results: A total of 23 components of MST were identified. The formulation was found to alleviate metabolic disorders, obesity, insulin resistance, inflammation, and oxidative stress in mice with MAFLD. The findings indicate that MST promoted autophagy by suppressing phosphorylation in the PI3K/AKT/mTOR pathway and enhancing lipid management in the livers of MAFLD mice.

Conclusion: MST could effectively improve lipid metabolism disorders and liver lipid deposition in MAFLD mice, and its mechanism might be related to regulating the PI3K/AKT/mTOR pathway to improve autophagy.

Keywords: modified Suanmei-Tang, MAFLD, transcriptomics, network pharmacology, metabolomics

Introduction

Metabolic-associated fatty liver disease (MAFLD) affects roughly 25% of people worldwide and is a major factor in the development of cirrhosis and liver cancer.[1] However, due to the extremely complex etiology and pathogenesis of MAFLD, there is a lack of targeted pharmaceutical interventions. The multiple-hit hypothesis offers insight into the genesis and advancement of MAFLD, positing that genetically predisposed individuals experience a series of insults, including lipid toxicity, insulin resistance (IR), mitochondrial and endoplasmic reticulum dysfunction, oxidative stress, and disrupted autophagy and inflammasomes.[2,3] Furthermore, numerous research findings have shown that disruptions in

Received: 29 July 2024
Accepted: 29 October 2024
Published: 13 November 2024

Graphical Abstract

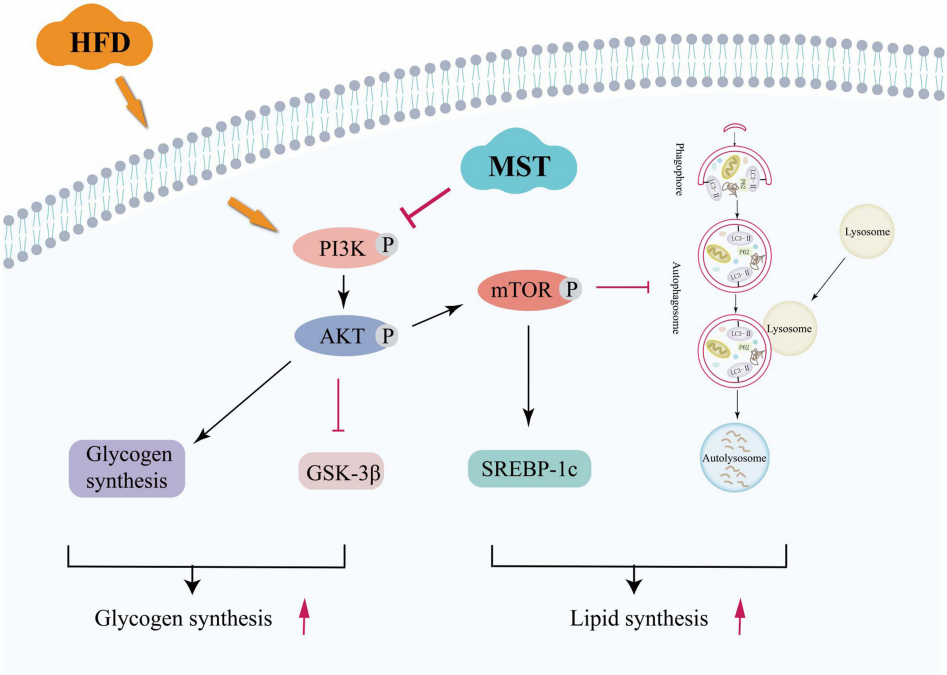

liver lysosomes and autophagy are connected to steatosis in MAFLD at the organ and cellular levels, highlighting autophagy as a promising therapeutic target.[4,5]

Traditional Chinese medicine (TCM) is characterized by unique therapeutic methods that are vital for promoting health and addressing diseases. TCM formulas typically consist of a combination of herbs that produce synergistic effects, resulting in favorable therapeutic results. Numerous TCM recipes have demonstrated beneficial outcomes in MAFLD cases, specifically by improving lipid metabolism and reducing inflammation, oxidative damage, and cellular death and decay.[6,7] Modified Suanmei-Tang (MST), a well-known traditional Chinese medicine blend, consists of Wumei (Prunus mume [Sieb.] Sieb. et Zuce), Shanzha (Crataegus pinnatifida Bunge), Chenpi (Citrus reticulata Blanco), and Gancao (Glycyrrhiza uralensis Fisch). Modern pharmacology has indicated that Wumei, Chenpi, and Gancao exhibit potent anti-inflammatory and antioxidant properties, thus mitigating tissue damage.[8–10] Additionally, Shanzha has been shown to ameliorate HFD-induced endothelial dysfunction by facilitating lipid expulsion, inhibiting cholesterol synthesis, suppressing preadipocyte differentiation, and affecting secretion factors.[11] Therefore, this study was conducted to further investigate the effects and underlying mechanisms of MST in addressing MAFLD.

With the widespread application of big data and artificial intelligence, modern bioinformatics technologies transcend the limitations of existing traditional methodologies and provide new ideas for medical research. Transcriptomics, which is the examination of gene transcription and its regulatory processes on a global scale, plays a crucial role in analyses of cellular phenotype and functionality. Network pharmacology is an experimental method for designing multitarget drugs; it involves selecting specific signal nodes through a network analysis of biological systems. Metabolomics involves a comprehensive quantitative analysis of all metabolites within an organism to elucidate the associations between metabolites and physiological or pathological alterations. Contemporary bioinformatics tools align with the multicomponent, multitarget, and multipathway nature of TCM formulations, providing new methods for exploring the therapeutic mechanisms of TCM in disease treatment.

In this research, the impact of MST on mouse models with MAFLD induced by an HFD was analyzed by monitoring serum and liver lipid metabolism indices. The primary mechanism through which MST treats MAFLD was investigated

using network pharmacology and transcriptomics and confirmed through real time quantitative PCR (RT-qPCR), Western blot (WB), molecular docking, and metabolomics. This approach clarified the function of MST in MAFLD management.

Materials and Methods

MST Preparation

The MST mixture included 30 g of Wumei, 30 g of Shanzha, 10 g of Chenpi, and 5 g of Gancao. These ingredients were sourced from the Affiliated Hospital of Chengdu University of Traditional Chinese Medicine and met the standards of the Pharmacopoeia of the People's Republic of China. The concoction was soaked in water for 20 min, maintaining a medicine-to-water ratio of 1:5 (g/mL). Following this, the medicine was boiled for 60 min, and then filtered using two layers of gauze. A second decoction was prepared with a 1:2.5 (g/mL) ratio, and the boiling process was repeated. After two rounds of boiling, the filtrate was added to form a 562.5 mL mixture, which was then rotated, evaporated, concentrated, and freeze-dried at 60 °C. The freeze-dried powder was sealed and stored at 4 °C in a refrigerator. This powder comprised a concentration of 5.17 g/g of raw herbs.

UHPLC-Q-Orbitrap-MS/MS of MST

To determine the main constituents in the freeze-dried MST powder, we conducted an analysis using UltiMate 3000 RS (Thermo Fisher Scientific, China). The analytical setup included an AQ-C18 chromatographic column by Welch, measuring 150×2.1 mm with a particle size of 1.8 μm and a flow rate of 0.30 mL/min. The mobile phase consisted of a 0.1% formic acid solution in water, and the organic phase consisted of methanol; methanol was also used for needle washing. The column was kept at 35 °C, and the autosampler was cooled to 10 °C. The samples were injected at a volume of 5 μL. Detection was performed using a Q Exactive high-resolution mass spectrometer (Thermo Fisher Scientific, China) equipped with an electron spray ionization interface that could operate in both positive and negative ion modes. The mass spectrometry settings included a full mass/dd-MS2 detection method, with resolutions of 70000 (full mass) and 17500 (dd MS2), covering a scan range of 150–2000 m/z. The electrospray voltage was adjusted to 3.8 kV in the positive mode, and the capillary temperature was maintained at 300°C. Argon gas (purity ≥ 99.999%) was used as the collision gas at a collision energy of 30, and nitrogen (purity ≥ 99.999%) was used as the sheath gas at 40 Arb, with the auxiliary gas heater set at 350 °C. Data collection spanned 30 min, and analysis was initially conducted using CD2.1 software (Thermo Fisher), with further comparisons conducted with the mzCloud database.

Animals, Drugs, and Reagents

Male C57bl6 J mice, aged six weeks and weighing 19–20 g, were acquired from Sperford (Beijing) Biotechnology Co., Ltd. (Animal Certificate Number: SCXK [Beijing] 2019–0010). This study was conducted in compliance with the Animal Experiment Ethics Code 2022–12 and was sanctioned by Chengdu University of Traditional Chinese Medicine. The mice were kept in a regulated environment at a temperature of 22–24 °C and a humidity level of 40–60%, with consistent lighting conditions. They had unrestricted access to food and water. The dietary regimen for the mice included high-fat feed (D12451, 45% kcal fat) and standard feed sourced from Xiaoshu Youtai (Beijing) Biotechnology Co., Ltd. Metformin (Met) was obtained from Jiangsu Chia Tai-Tianqing Pharmaceutical Co., Ltd. Essential biochemical reagents were purchased from different suppliers: cholesterol (CHO) from Meikang Biotechnology Co., Ltd.; non-esterified fatty acids (NEFAs) from Changchun Huili Biotech Co., Ltd.; insulin (INS) from Elabscience Biotechnology Co., Ltd.; tumor necrosis factor-alpha (TNF-α) from Sino Biological Inc.; interleukin-1 beta (IL-1β) from MultiSciences Biotech Co., Ltd.; malondialdehyde (MDA) from Wuhan Servicebio Technology Co., Ltd.; and superoxide dismutase (SOD) and glutathione peroxidase (GSH-Px) from Nanjing Jiancheng Technology Co., Ltd. The proteins and antibodies used in this study were acquired from the following companies: recombinant human beclin 1 protein (Beclin 1) and microtubule-associated protein light chain 3 I (LC3 I) from Abcam PLC; microtubule-associated protein light chain 3 II (LC3II) from Beijing Bioss Biotechnology Co., Ltd.; sequestosome 1 (P62) from Wuhan Servicebio Technology Co., Ltd.; β-Actin from Aibokang (Shanghai) Trading Co., Ltd.; AKT from Shenyang Wanlei Biotechnology Co., Ltd.; p-AKT from Santa Cruz Biotechnology; mTOR and p-mTOR from Wuhan Sanying Biotechnology Co., Ltd.; PI3K from Absin Bioscience

Inc.; and phosphorylated PI3K from Affinity Bioscience. Additionally, HRP-conjugated goat anti-rabbit and HRP-conjugated goat anti-mouse antibodies were sourced from Wuhan Yilairuite Biotechnology Co., Ltd.

Animal Experiment Design

Following a week-long acclimatization period, the control group was fed a regular diet, whereas the other groups were placed on an HFD for 12 weeks to develop MAFLD mouse models. The criteria for a typical MAFLD mouse model include a marked increase in body weight and a liver that exhibits an irregular yellow or reddish-yellow coloration, along with an increase in liver weight and serum triglyceride levels, a decrease in HDL cholesterol levels, an appreciable increase in liver size, blunted liver edges, and a softer liver texture. Histologically, liver sections tend to have a greasy appearance, and hematoxylin and eosin (H&E) staining reveals significant lipid droplet accumulation in the liver cells.[12] After establishing the MAFLD models in line with these criteria, the mice were divided into six groups (each containing six mice): Control, Model, High-Dose MST (MST-H), Medium-Dose MST (MST-M), Low-Dose MST (MST-L), and Metformin (Met). The MST dosages, which were adjusted for body surface area using Km values of 3 for mice and 37 for humans, were established at 2.2 g/kg, 1.1 g/kg, and 0.55 g/kg. Metformin was administered at 0.1 g/kg. The control and model groups were given saline orally on a daily basis. All treatments were administered at a volume of 10 mL/kg daily over a period of eight weeks. After the treatment phase, the mice underwent a 24 h fasting period and were then anesthetized with pentobarbital. Blood was drawn from an eyeball of each mouse and collected in 2 mL centrifuge tubes, which were then spun at 3500 rpm for 10 min. The serum was extracted and preserved at −20 °C. Simultaneously, liver tissue was divided into five parts. A segment of liver tissue was fixed in 4% paraformaldehyde, while four other liver tissue samples were quickly frozen using liquid nitrogen and then stored at −80 °C in prelabeled, chilled cryotubes.

Measurement of Body Weight, Liver Weight, and Liver Index

Mouse weights were recorded weekly. The mice were first weighed after anesthesia administration, prior to blood collection from the eyeball. Following this, euthanasia was performed using the spinal dislocation method. The livers were then excised and rinsed with saline, and surface moisture was absorbed using filter paper before weighing the livers. The liver index for each sample was calculated using the following formula: liver index = (liver weight [g] / body weight [g]) * 100%.

Biochemical Indicators and ELISA Detection

The triglyceride (TG), low-density lipoprotein cholesterol (LDL-C), high-density lipoprotein cholesterol (HDL-C), alanine aminotransferase (ALT), aspartate aminotransferase (AST), and glucose contents in serum were measured using a fully automated biochemical analyzer in accordance with the manufacturer's guidelines. Further, insulin, CHO, and NEFA contents in the serum samples were measured using specific ELISA kits. For liver tissue analyses, liver tissue was homogenized in a 1:9 weight-to-volume ratio of phosphate buffered solution (PBS) under ice-cold conditions. After homogenization, the mixture was centrifuged at 12,000 rpm for 10 min at 4 °C and the resulting supernatant was collected. The SOD, MDA, GSH-Px, TNF-α, and IL-1β levels of the liver tissues were quantified using ELISA kits, according to the instructions provided.

H&E Staining and Oil Red O Staining

The liver tissue sample preserved in 4% paraformaldehyde was washed with distilled water and submerged in 75% ethanol overnight. After undergoing dehydration, clearing, and paraffin embedding, the tissues were sectioned and mounted for H&E staining. For Oil Red O staining, the liver tissue was first infused with an optimum cutting temperature compound and then sectioned in their frozen state. The liver tissue samples obtained from each group of mice were analyzed under a light microscope. Furthermore, Image J Pro Plus software was used to evaluate the sections stained with H&E and Oil Red O.

Transcriptomic Analysis of Liver Tissue

Total RNA was extracted from liver tissues of the Control, Model, and MST-H groups using the RNArep Pure Tissue Kit. Following this, mRNA containing polyA tails was isolated using Oligo(dT) magnetic beads, fragmented, and used to

generate first- and second-strand cDNA. Following poly(A) tail addition, sequencing adapters were affixed, and PCR amplification was performed to construct a library. The insert sizes were quantified and assessed using a Qubit 2.0 Fluorometer and an Agilent 2100 bioanalyzer. After library validation, different libraries were pooled for Illumina sequencing based on the required concentration and target data volume. Fast[13] was used to meticulously ensure data integrity and produce high-quality, clean reads for subsequent analyses. HISAT2[14] was used to align these clean reads with the reference genome, while featureCounts v1.6.2 was utilized to quantify gene alignment, with the Fragments Per Kilobase of exon model per Million mapped fragments for each gene computed based on gene length. DESeq2 was used to conduct differential expression analysis across groups, pinpointing genes that varied significantly between two biological conditions. Following this, the Benjamini–Hochberg method was applied to adjust the *P* values for multiple hypothesis testing, resulting in the calculation of the false discovery rate (FDR). Differential gene selection criteria were $|\log2\text{Fold Change}| \geq 1$ and $\text{FDR} < 0.05$. Enrichment analyses of the identified genes were then performed using the Kyoto Encyclopedia of Genes and Genomes (KEGG) databases to delve into their associations with various biological pathways.

Network Pharmacology

The compounds in MST, which were identified via UHPLC-Q-Orbitrap-MS/MS, were subjected to target prediction using SwissADME (http://www.swissadme.ch/). Disease-related targets were gathered from diverse sources, including GeneCards (https://www.genecards.org/ds), OMIM (https://omim.org/), Drugbank (http://go.Drugbank.com/), TTD (http://db.idrblab.net/ttd/), and PharmGKB (https://www.pharmgkb.org/). According to the *Ethical Review Measures for Life Science and Medical Research Involving Humans*, the public database used in this study can be exempted from ethical review.[15] After eliminating duplicates, the microbiome platform (https://www.bioinformatics.com.cn/) was used to perform KEGG enrichment analyses of the common genes. These analyses were aimed at unveiling the potential functionalities of the genes. A significance threshold of $P < 0.05$ was applied to identify relevant GO terms and KEGG pathways.

Metabolomic Analysis of Liver Tissue

Liver tissue samples from the Control, Model, and MST-H groups, each weighing 20 mg, were homogenized and centrifuged at 3000 rpm and 4 °C for 30 sec. Following this, 400 μL of a 70% methanol–water solution containing an internal standard was added. The mixture was vigorously shaken at 1500 rpm for 5 min and then incubated on ice for 15 min. Centrifugation was subsequently performed at 12000 rpm and 4 °C for 10 min, and the samples were then chilled at −20 °C for 30 min. After a final centrifugation at 12000 rpm and 4 °C for 3 min, 200 μL of the clear supernatant was transferred into an injection vial for subsequent analysis. To ensure the reproducibility of the analysis, quality control (QC) samples were created by mixing extracts from different samples and processing them under uniform conditions.

Metabolite analysis was performed using UHPLC-MS/MS. Chromatographic separation was achieved with a Waters ACQUITY UPLC HSS T3 C18 1.8 μm, 2.1 mm x 100 mm column. The mobile phase was divided as follows: the A phase consisted of ultrapure water with 0.1% formic acid, and the B phase consisted of acetonitrile with 0.1% formic acid. The elution profile began with a water-to-acetonitrile ratio of 95:5 at 0 min, which shifted to 10:90 at 11 min and was maintained until the 12^{th} min, then returned to 95:5 at 12.1 min and was maintained until the 14^{th} min. The flow rate was set at 0.4 mL/min with a column temperature of 40 °C and an injection volume of 2 μL. Mass spectrometry was conducted using an ESI source at 5500 V for positive ion modes and −4500 V for negative ion modes. Source gases I and II were regulated at 55 psi and 60 psi, respectively, with a curtain gas at 25 psi. High collision-induced ionization settings were applied. In the triple quadrupole (Qtrap) system, each ion pair was meticulously scanned and detected, and the cluster potential and collision energy were fine-tuned for each analyte.

The metware database was used to perform a qualitative analysis of the metabolites, focusing on retention time, parent–daughter ion pairs, and secondary spectral information. For the quantitative analysis, the multiple reaction monitoring mode in Qtrap was utilized. Metabolite peak integration and calibration were performed using MultiQuant software, with all peak area integration data subsequently exported and saved. The mass spectrometry data were processed using Analyst 1.6.3 software; the tasks included the identification, alignment, filtering, and normalization of

peak areas. To explore between- and within-group differences in metabolite profiles, multivariate analyses, such as principal component analysis (PCA) and partial least squares discriminant analysis, were employed. Additionally, the significance of each variable was assessed using the variable importance in projection (VIP) scores derived from the orthogonal partial least squares-discriminant analysis (OPLS-DA) model. Metabolites showing significant differences were pinpointed by integrating the VIP scores, fold changes, and *P* values derived from the OPLS-DA model, using a threshold of VIP ≥ 1 and $P < 0.05$ for the selection.

Quantitative Reverse Transcription Polymerase Chain Reaction (RT-qPCR)

Total RNA was extracted from liver tissue specimens using a Total RNA Miniprep Kit. Subsequently, cDNA was produced using a reverse transcription kit, according to the given instructions, which was then utilized for the fluorescence quantitative PCR assays. The PCR setup involved initial denaturation at 95 °C for 5 min, followed by cycling at 95 °C for 10 sec and 60 °C for 30 sec, and ending with a gradual increase from 65 °C to 95 °C at a rate of 0.5 °C every 5 sec. Post reaction, the Ct values of the target and internal reference genes were obtained for the control and experimental groups. Gene expression quantification was performed using the 2^-ΔΔCt method. Specific details on the primer sequences are provided in Table 1.

Table 1 Primer Sequences

Target gene	FORWARD/REVERSE (F/R)	Primer sequence	Product length/(bp)
β-actin	F	CCTCACTGTCCACCTTCC	120
	R	GGGTGTAAAACGCAGCTC	
TNF-α	F	GAAACACAAGATGCTGGGA	120
	R	TTGCAGAACTCAGGAATGG	
SREBP1c	F	CAGACTCACTGCTGCTGACA	119
	R	GATGGTCCCTCCACTCACCA	
HMGCR	F	AGAGAACAAGGGTTCACGCC	104
	R	CCTTGGATCCCACGCGGA	
INSR	F	ATGGGCTTCGGGAGAGGAT	214
	R	CTTCGGGTCTGGTCTTGAACA	
GSK3β	F	ATGGCAGCAAGGTAACCACAG	193
	R	TCTCGGTTCTTAAATCGCTTGTC	
CCR2	F	GCCATAGGCCCTTTTGTGTTG	141
	R	TGGGTTGGAAGAAGCACAGT	
Cx3cr1	F	TCTTCACGTTCGGTCTGGTG	80
	R	GTCAGTGATGCTCTTGGGCT	
Fabp4	F	TGGGATGGAAAGTCGACCAC	190
	R	CTTCCTTTGGCTCATGCCCT	
Cidec	F	GGGGGAGGTCCAACACAATC	186
	R	GATCTGCGGTGCTAACACGA	
Col1a2	F	CTAGCCAACCGTGCTTCTCA	70
	R	TCTCCTCATCCAGGTACGCA	
Col1a2	F	AGCACGTCTGGTTTGGAGAG	112
	R	GACATTAGGCGCAGGAAGGT	
Acot1	F	AGTGCTGATTCAAGGGCTGG	89
	R	TTCTCGCAGCTGGATTGAAC	
Acot4	F	CCACATTGGCTCTGGCTTTT	101
	R	TCGAAGCATGTACCGCACTG	
SMPD3	F	TGGGAAAGCTGAGGTGGTATAG	105
	R	GTTCGCTTCAAGGGGCCAT	
Spp1	F	CTCGGAGGAAACCAGCCAAG	80
	R	AGTTAGTCCCTCAGAATTCAGCC	

(*Continued*)

Table 1 (Continued).

Target gene	FORWARD/REVERSE (F/R)	Primer sequence	Product length/(bp)
Cxcl14	F	GTAAGTGTTCCCGGAAGGGG	84
	R	CCTCGCAGTGTGGGTACTTT	
IL-1β	F	TGTCCTGATGAGAGCATCC	128
	R	AAGGTCCACGGGAAAGAC	
SYNJ2	F	GCGTTCTGTGGGAAGGTCTA	114
	R	CTCACACCCACGCGAAAAAG	
CYP7A1	F	TGATCTGGGGGATTGCTGTG	95
	R	CCCGTTGTCCAAAGGAGGTT	

Immunohistochemistry

The liver tissues were initially preserved in 4% paraformaldehyde and then embedded in paraffin for section preparation. The tissue sections were processed for immunohistochemistry (IHC), starting with the application of primary antibodies, followed by secondary antibodies tagged with horseradish peroxidase. The sections were stained using a diaminobenzidine reagent kit and then counterstained with hematoxylin. Finally, the pathological sections were visualized and captured using a microscope equipped with a pathological section scanner.

Western Blot

For protein extraction, 100 mg of liver tissue was processed with a tenfold volume of RIPA lysis buffer. Homogenization, lysis, and centrifugation were conducted to acquire the total protein extract. The protein concentrations were then quantified using the bicinchoninic acid assay. The proteins were separated via sodium dodecyl sulfate – polyacrylamide gel electrophoresis and transferred onto polyvinylidene fluoride membranes at a constant current of 200 mA for 1 h. The membranes were blocked in TBST containing 5% skim milk for 1 h, followed by overnight incubation with primary antibodies and subsequent incubation with secondary antibodies. The protein bands were visualized and analyzed using Alpha Ease FC software.

Molecular Docking

For molecular docking, we focused on three overactivated class I PI3K catalytic subunit p110 subtypes (α, β, and γ), along with AKT1, AKT2, and mTOR. The primary structures of the proteins were obtained from the RCSB Protein Data Bank (PDB) (http://www.rcsb.org/) using the specific protein file IDs provided: PI3K α (4ZOP), PI3K β (4J6I), PI3K γ (3L54), AKT1 (3MVH), AKT2 (3D0E), and mTOR (4JT6); all these proteins interact with ATP competitive inhibitors. Three-dimensional models of the ligand molecules were sourced from the PUBCHEM database (https://pubchem.ncbi.nlm.nih.gov/). Docking simulations were conducted using cb dock2 (https://cadd.labshare.cn/cb-dock2/php/blinddock.php#job_list_load).[16]

Statistical Analysis

Data analysis and visualization were carried out using GraphPad Prism 9.5. Quantitative data were expressed as mean ± standard deviation ($\bar{x} \pm S$) values. For two-group comparisons, the least significant difference test was used for data following a normal distribution, while the Mann–Whitney *U*-test was applied to data that did not follow a normal distribution. For comparisons of multiple groups, a one-way ANOVA was used when the variance was equal, and Dunnett's T3 test was used when the variances were unequal. Statistical significance was determined at $P < 0.05$.

Results

MST Components and Targets

Positive and negative ion scans revealed 23 components of MST, including Nicotinic acid, Citric acid, Kasugamycin, Benzoic acid, Chlorogenic acid, Caffeic acid, Naringenin, 2.6-Dimethoxyphenol, Isoliquiritigenin, Rutin, Limonin, Naringin, Hesperidin, Quercetin, Formononetin, Ononin, 5.7-Dihydroxy-2-(3-hydroxy-4-methoxyphenyl)chroman-4-one, Genistein, Nobiletin, Myristic acid, Linoleic acid, Palmitic acid, Stearic acid (Figure 1).

Effects of MST on Obesity and Lipid Metabolism

Obesity and dyslipidemia are key risk factors for MAFLD. Our study involved inducing MAFLD in mice through 12 weeks of HFD feeding, leading to significant weight gain and lipid metabolism disorders. For eight weeks, the MST and Met groups were treated with oral administrations of MST at dosages of 0.55, 1.1, and 2.2 g/kg/day and metformin at 0.1 g/kg/day, respectively (Figure 2A). Both MST and metformin significantly reduced the body weights of mice fed the HFD (Figure 2B and C). The TG, LDL-C, and HDL-C contents in serum were measured using a fully automated biochemical analyzer. Additionally, CHO and NEFA levels were determined via ELISA. Compared to the Model group, the MST group exhibited marked reductions in TG, LDL-C, CHO, and NEFA content levels and significantly increased HDL-C levels (Figure 2D). These findings are indicative of MST's efficacy in improving the lipid metabolism and reducing the body weights of MAFLD mice.

Effects of MST on IR and Liver Lipid Deposition

Insulin's role in liver lipid metabolism, specifically in facilitating new fat generation, hindering fatty acid oxidation, and promoting triglyceride synthesis, can contribute to metabolic liver disorders. Due to the buildup of lipid droplets in the liver cells of the MAFLD mice—a key indicator of fatty liver—we explored the impact of MST on IR and lipid accumulation in the mouse livers. Biochemical and ELISA techniques were used to assess blood sugar and insulin levels and thereby compute the IR indexes. Liver pathology was examined using H&E and Oil Red O staining methods, and the liver weights and liver indexes were assessed. The mRNA expression levels for genes associated with lipid synthesis (SREBP-1c),

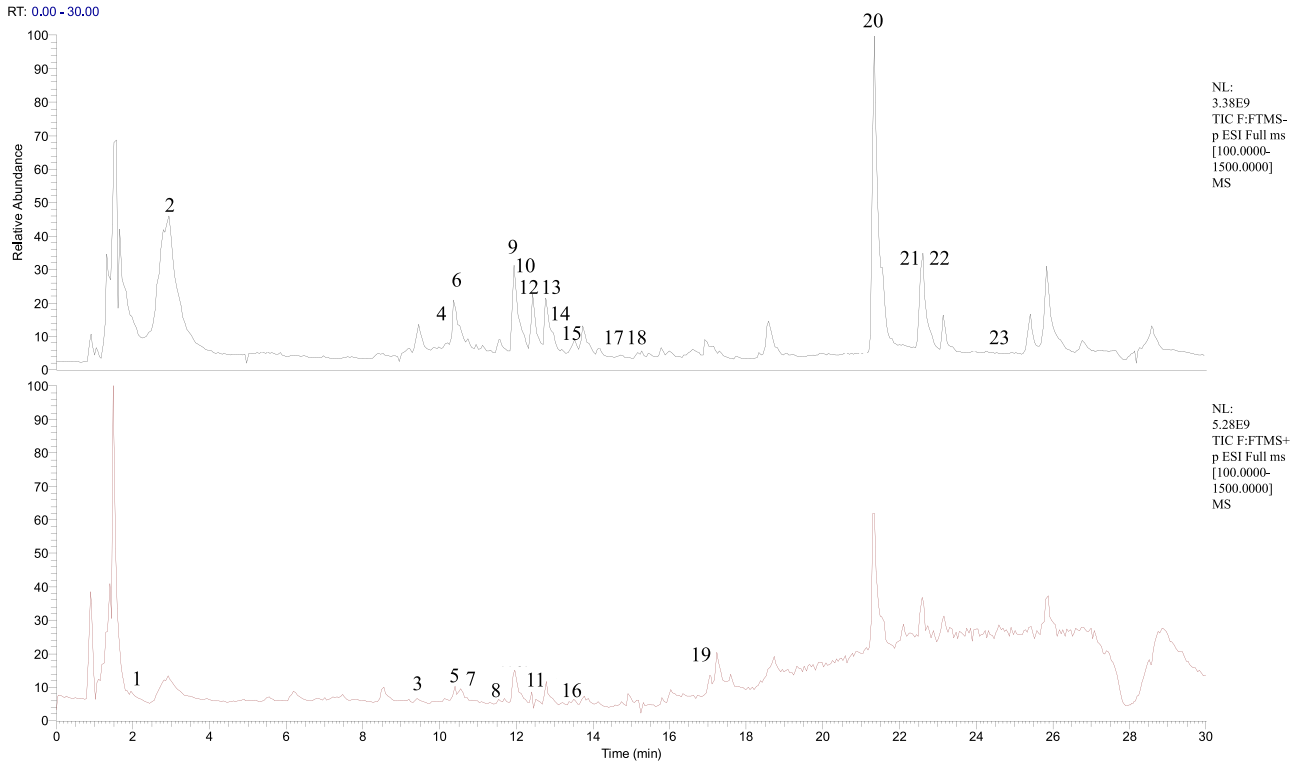

Figure 1 Total ion current diagram in positive and negative modes.

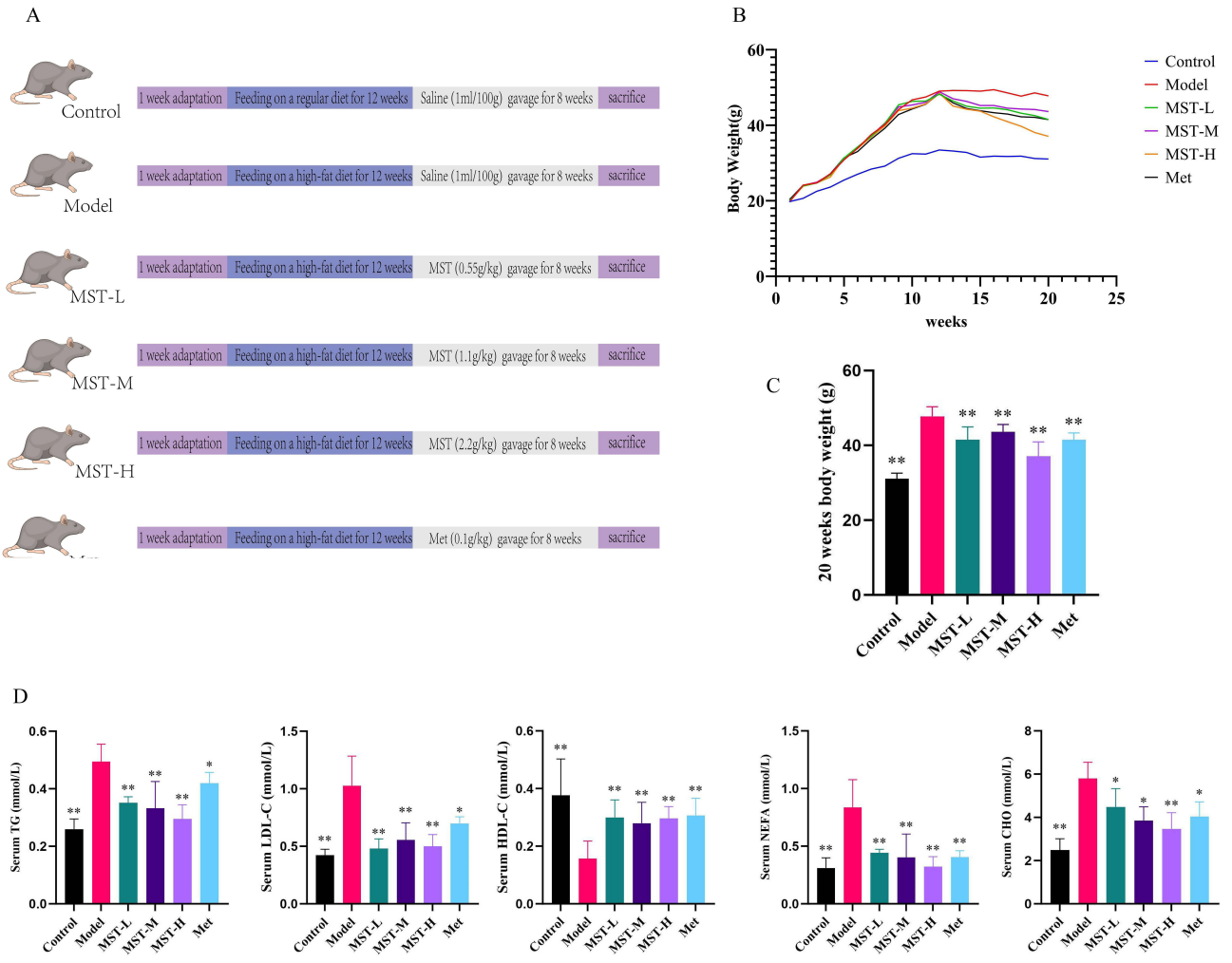

Figure 2 Effects of MST on obesity and lipid metabolism. (**A**) Protocol of the animal experiments. (**B**) Line chart of the body weights of the mice. (**C**) Body weights of the mice. (**D**) Effects of MST on serum lipids in the HFD mouse models. n = 6. The results are expressed as mean ± SD values. Compared to the Model group, *$p < 0.05$, **$p < 0.01$.

cholesterol synthesis (HMGCR), and glycogen synthesis (INSR, GSK-3β) were analyzed using RT-qPCR. ELISA was used to gauge the liver lipid metabolism markers (TG, NEFA, and CHO) and insulin levels. Compared to the Control group, the model mice had elevated blood sugar, insulin levels, and IR indexes. MST and metformin mitigated these effects by modulating GSK-3β and INSR mRNA levels (Figure 3A and B), thereby reducing glycogen synthesis. Further, the liver tissues of the model mice exhibited increased cell size, lipid droplets, inflammation, and NAS scores when compared to those of the controls. Oil Red O staining indicated a notable accumulation of liver lipids in the Model group. In contrast, the MST-treated groups had significantly reduced liver weights, liver indexes, and mRNA levels of SREBP-1c and HMGCR genes as well as low levels of TG, NEFA, and CHO compared to the Model group (Figure 3C–H). These results underscore the effectiveness of MST in reducing IR and liver lipid accumulation in the MAFLD mice.

Impact of MST on Inflammation, Oxidative Stress, and Autophagy

MAFLD is characterized by excessive triglyceride storage, with inflammation, oxidative stress, and autophagy contributing to its development. To evaluate the effects of MST on these factors in the MAFLD mice, the TNF-α and IL-1β levels of the mouse livers were determined using both ELISA and RT-qPCR. The ALT and AST levels were quantified using an automated biochemical analyzer, and the oxidative stress markers (SOD, MDA, and GSH-Px) were evaluated via ELISA. Autophagy-related indicators, including Beclin-1, P62, LC3 II, and LC3 I, were detected through IHC. Compared to the

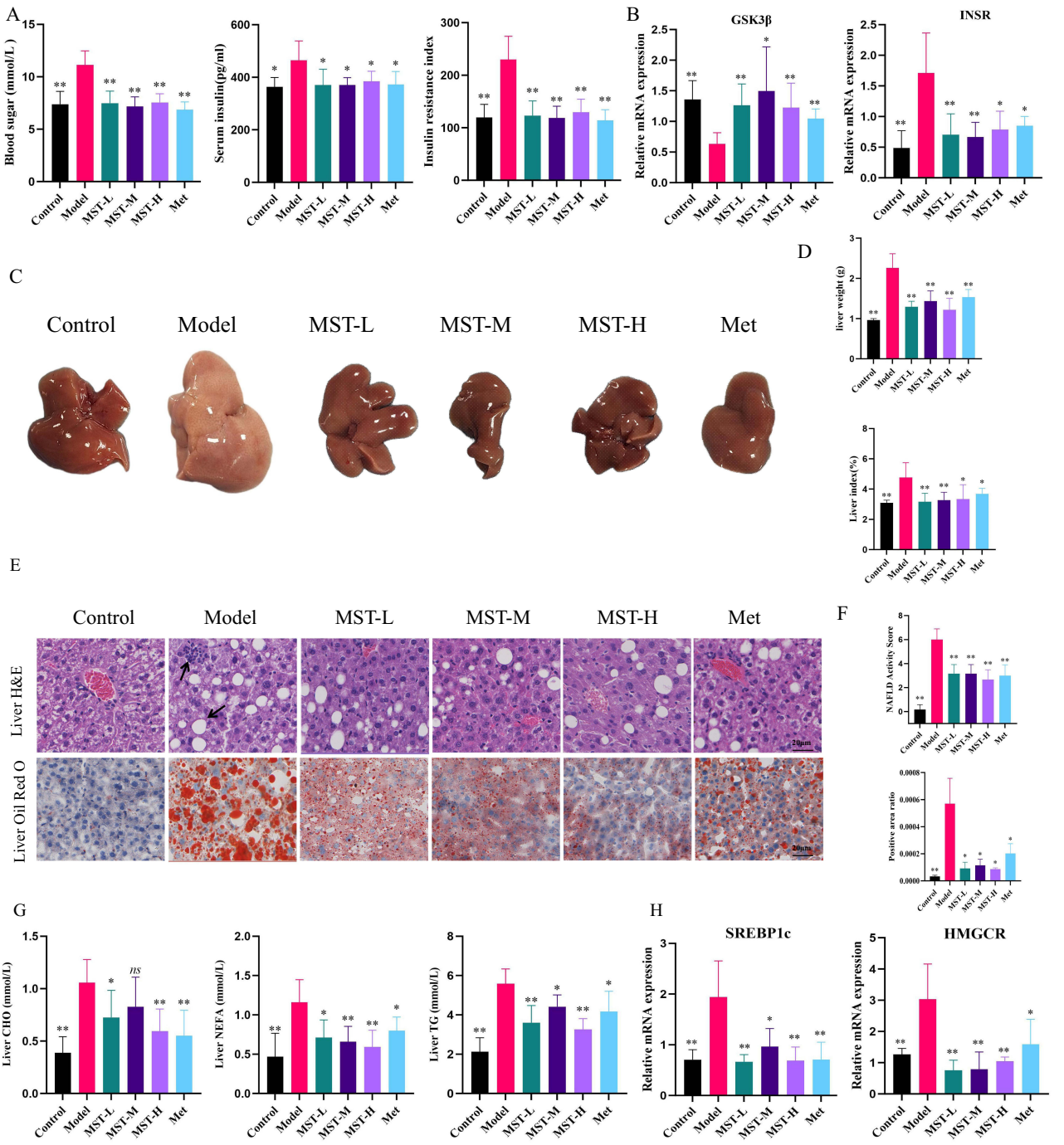

Figure 3 Effects of MST on IR and liver lipid deposition. (**A**) Effects of MST on the blood sugar, insulin, and IR indexes of the MAFLD mouse models. (**B**) Effects of MST on the relative mRNA levels of GSK-3β and INSR. (**C**) Macroscopic appearance of the mouse livers in each group. (**D**) Effects of MST on the liver weights and liver indexes of the mice, n = 6. (**E** and **F**) Effects of MST on the hepatic pathological changes in the MAFLD mouse models (×200), n = 5. (**G**) Effects of MST on the liver TG, NEFA, and CHO of the MAFLD mouse models. (**H**) Relative mRNA levels of SREBP1c and HMGCR, n = 6. The results are expressed as mean ± SD values. Compared to the Model group, *$p < 0.05$, **$p < 0.01$, *ns*: not significant.

Model group, the MST-treated groups demonstrated substantial reductions in liver TNF-α and IL-1β levels and serum AST and ALT levels (Figure 3A–C). In addition, the liver MDA levels were lower in the MST-treated groups, while the SOD and GSH-Px levels increased (Figure 4D). The expression levels of LC3-I and P62 positive cells decreased, whereas Beclin-1 and LC3-II positive cells were more prevalent in the MST-treated groups (Figure 4E). These findings indicate that MST effectively reduced inflammation and oxidative stress and enhanced autophagy in the MAFLD mice.

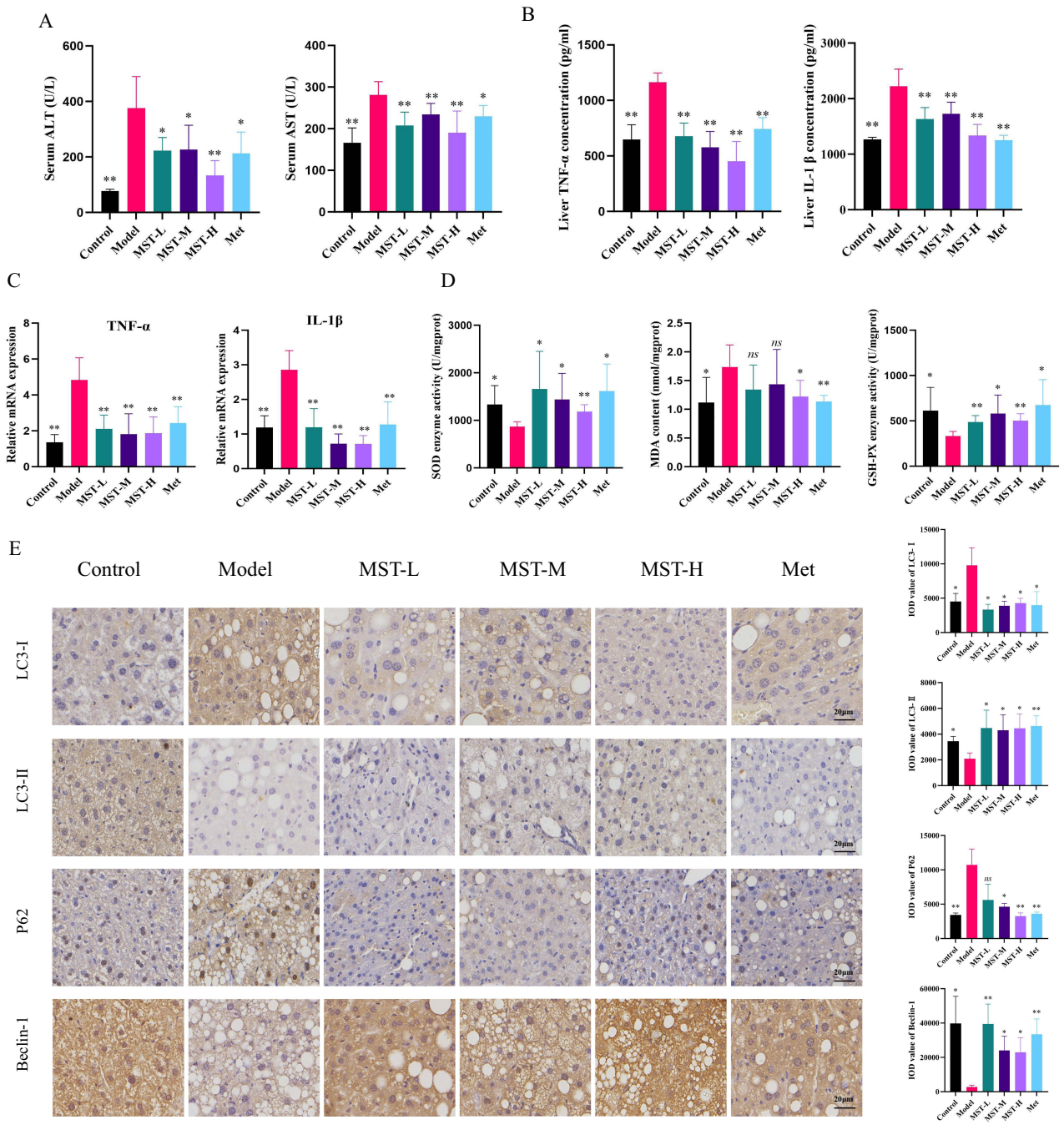

Figure 4 Effects of MST on inflammation, oxidative stress, and autophagy. (**A**) Effects of MST on the serum ALT and AST levels of the MAFLD mouse models. (**B**) Effects of MST on the liver TNF-α and IL-1β levels of the MAFLD mouse models. (**C**) Effects of MST on the relative mRNA levels of TNF-α and IL-1β in the MAFLD mouse models. (**D**) Effects of MST on the liver SOD, MDA, and GSH-PX of the MAFLD mouse models, n = 6. (**E**) Effects of MST on the Beclin-1, P62, LC3-II, and LC3-I expression levels of the MAFLD mouse models (×200), n = 5. The results are expressed as mean ± SD values. Compared to the Model group, *$p < 0.05$, **$p < 0.01$, *ns*: not significant.

Transcriptomic Analysis of the MST Intervention

To evaluate the impact of MST on liver gene expressions in MAFLD mice, transcriptomic analyses were performed with samples from the Control, Model, and MST-H groups. A PCA demonstrated a clear separation between the Model and Control groups, with significant changes in gene expression due to the conditions of the mouse models. The MST-H group was positioned between these two groups, indicating a postintervention normalization of gene expression (Figure 5A). With FDR < 0.05 and | log2Fold Change| ≥ 1 as the thresholds, a total of 1127 differentially expressed genes (DEGs) between the Control and Model groups were identified, including 734 upregulated genes and 393 downregulated genes. A comparison of the Model and MST-H

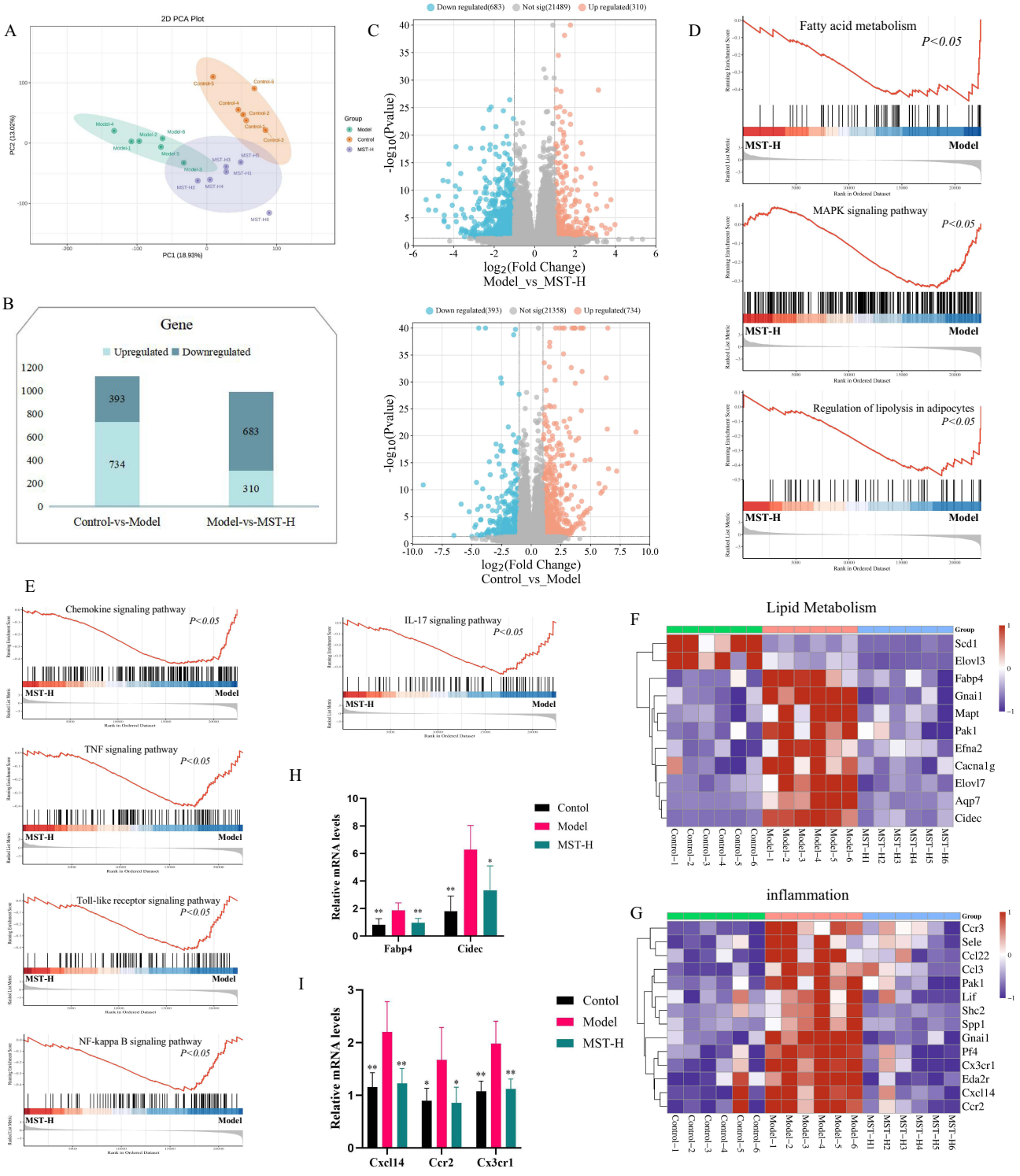

Figure 5 Transcriptomic analysis of the MST intervention. (**A**) Scatter plot of liver transcriptome scores for the control group, model group, and MST-H group, as determined by PCA. (**B**) Number of differentially expressed genes in two comparisons, with the light blue color representing upregulated genes and the dark blue color representing downregulated genes. (**C**) Volcano map of the DEGs in the control group vs the model group and the model group vs the MST-H group. (**D** and **E**) GSEA enrichment analysis of pathways related to lipid metabolism and inflammation. (**F** and **G**) Heat maps of gene expressions related to lipid metabolism and inflammation based on the RNA-seq data set, n = 6 per group. (**H**) Relative mRNA levels of lipid metabolism genes (Fabp4 and Cidec). (**I**) Relative mRNA levels of inflammation genes (Cxcl14, Ccr2, and Cx3cr1), n = 6. The results are expressed as mean ± SD values. Compared to the Model group, *$p < 0.05$, **$p < 0.01$.

groups revealed 993 DEGs, including 310 upregulated genes and 683 downregulated genes (Figure 5B and C). A gene set enrichment analysis (GESA) revealed an overall downregulation in signaling pathways related to lipid metabolism and inflammation in the MST-H treatment group (Figure 5D and E). In addition, heat maps demonstrated a reduction in genes associated with lipid metabolism and inflammation in the MST-H group (Figure 5F and G). Given that disturbances in lipid metabolism and inflammatory processes are crucial for the development of MAFLD, RT-qPCR was performed to verify the expression of genes related to lipid metabolism (Fabp4 and Cidec) and inflammation (Cxcl14, Ccr2, and Cx3cr1). The results supported the transcriptomic data, as illustrated in Figure 5H and I, suggesting that a high dose of MST modulated lipid metabolism and inhibited inflammatory responses in the MAFLD mice.

Transcriptomic studies and network pharmacology analysis results of potential pathways by which MST may treat MAFLD

To further explore the mechanisms by which the treatment outcomes of MST are enhanced in MAFLD cases, KEGG pathway analysis was conducted using transcriptomic data and network pharmacology for the Model and MST-H groups. Targets were extracted from the Swiss Target Prediction database and refined based on relevant literature, which resulted in 1748 select targets. Disease-related processes and inflammation, lipid metabolism, autophagy, PI3K-AKT, and mTOR pathways were significantly prominent (Figure 6A–D). Further, GSEA analysis and heat maps highlighted the capacity of MST-H to suppress gene expression linked to the PI3K-AKT pathway (Figure 6E and F). A subsequent RT-qPCR analysis validated the expression of PI3K-AKT pathway genes (Spp1, Col1a1, and Col1a2), corroborating the transcriptomic findings (Figure 6G).

Molecular Docking and WB Verification

MTOR is a crucial nuclear transcription factor that orchestrates various physiological processes, including metabolism and inflammation. The activation of the PI3K/AKT/mTOR signaling pathway, primarily through phosphorylation events, is known to contribute to metabolic disruptions and inflammation. Studies have shown that inhibiting PI3K/AKT/mTOR phosphorylation can regulate intracellular lipid metabolism, diminish inflammation, and stimulate autophagy.[17] To explore the impact of MST on the PI3K/AKT/mTOR pathway, naringenin, quercetin, formononetin, and nobiletin were chosen from the 23 active components identified in MST through UHPLC-Q-Orbitrap-MS/MS. These selections were based on their oral bioavailability (OB) of at least 30% and drug-likeness (DL) score of 0.18 or higher for molecular docking studies with PI3K/AKT/mTOR proteins. The docking results revealed negative minimum binding energies between these components and the pathway proteins; the highest was −6.4 kcal/mol, and nine binding modes were less than −8 kcal/mol (Figure 7A–J). This indicates that potential inhibitory interactions occurred at the protein ATP sites. The WB analysis showed that the PI3K, Akt, and mTOR phosphorylation levels were higher in the Model group than in the Control group (Figure 7K and L), suggesting that MST exerted a suppressive effect on the PI3K/AKT/mTOR signaling pathway.

Metabolomic Analysis of the MST Intervention in MAFLD Mice

To investigate the metabolic effects of MST, a nontargeted metabolomic analysis was performed. OPLS-DA was used to distinguish between metabolite profiles, revealing differences between the treatment and control groups, with R^2Y = 0.974 and Q^2 = 0.953 for the Control and Model groups, and R^2Y = 0.907 and Q^2 = 0.883 for the Model and MST-H groups, confirming the model's reliability. Permutation tests demonstrated the model's robustness and predictive capability without overfitting (Figure 8A and B). With VIP > 1 and $P < 0.05$ as the OPLS-DA criteria, 123 metabolites were detected across the Control, Model, and MST-H groups (Figure 8C and D) (Supplementary Table 1). Heat maps demonstrated a notable reversal of metabolic disturbances in the MST-H group compared to the Model group, indicating that a high dose of MST has the potential to regulate metabolic imbalances (Figure 8E). A KEGG analysis of differential metabolites revealed involvement in key pathways, including metabolism, lysine biosynthesis, and glyoxylate and dicarboxylic acid metabolism (Figure 8F), thus shedding light on the therapeutic mechanisms of MST in the MAFLD mice.

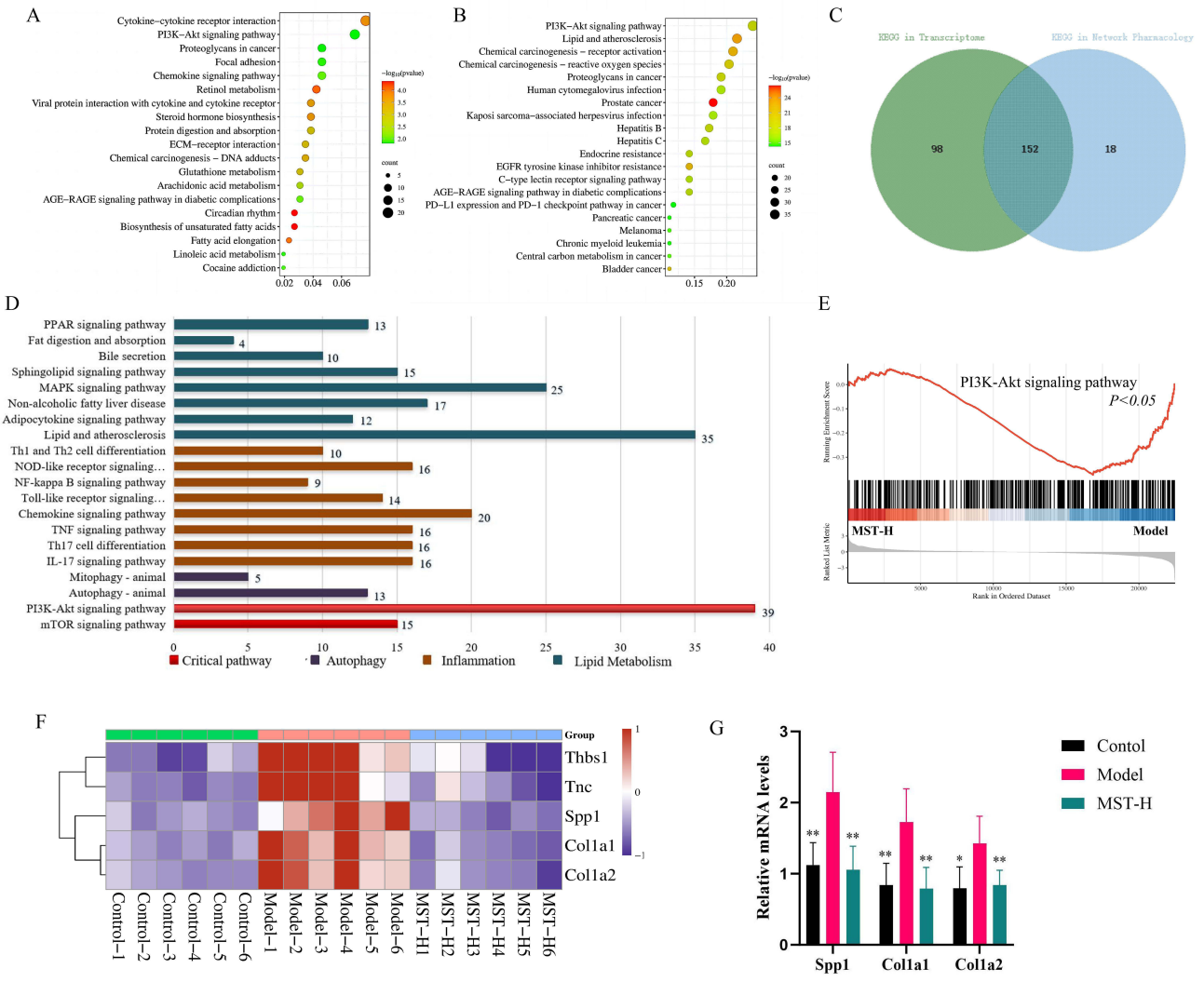

Figure 6 Transcriptomic studies and network pharmacology analysis results of potential pathways by which MST may treat MAFLD. (**A**) KEGG term pathway related to the liver and enriched by DEGs (Model vs MST-H) in transcriptomics. (**B**) KEGG term pathway related to the liver and enriched by DEGs (Model vs MST-H) in network pharmacology. (**C**) Venn diagram of the enriched KEGG term pathways in transcriptomics and network pharmacology. (**D**) Summary of the enriched KEGG term pathways in transcriptomics and network pharmacology. (**E**) GSEA enrichment analysis of pathways related to PI3K-Akt signaling pathway. (**F**) Heat maps of gene expressions related to the PI3K-Akt signaling pathway based on the RNA-seq data set. n = 6 per group. (**G**) Relative mRNA levels of PI3K-Akt signaling pathway genes (spp1, Col1a1, and Col1a2), n = 6. The results are expressed as mean ± SD values. Compared to the Model group, *$p < 0.05$, **$p < 0.01$.

Integrated Analysis of Transcriptomic and Metabolomic Data

To elucidate the role of MST in ameliorating MAFLD, Metscape software was used to integrate differential metabolites and DEGs. This resulted in the identification of five key targets—sphingomyelin phosphodiesterase 3 (SMPD3), synaptic janin2 (SYNJ2), acyl-coA thioesterase 4 (ACOT4), recombinant cytochrome p450 7A1 (CYP7A1), and acyl-coA thioesterase 1 (ACOT1) (blue hexagons in Figure 9A)—and eight pivotal metabolites—CMP, Choline phosphate, glycolithocholate, L-Lysine, FAD, Taurocholate, Taurolithocholate, Sphingosine 1-phosphate (red hexagons in Figure 9A). These components are involved in several key pathways, including bile acid biosynthesis, phosphatidylinositol phosphate metabolism, fatty acid metabolism, and glycerophospholipid metabolism. A subsequent heat map analysis of the key metabolites, coupled with RT-qPCR validation, confirmed that high-dose MST treatment effectively reversed the expression of SMPD3, SYNJ2, ACOT4, CYP7A1, and ACOT1 (Figure 9B and C). Collectively, these findings indicate that MST has protective and therapeutic potential in MAFLD cases.

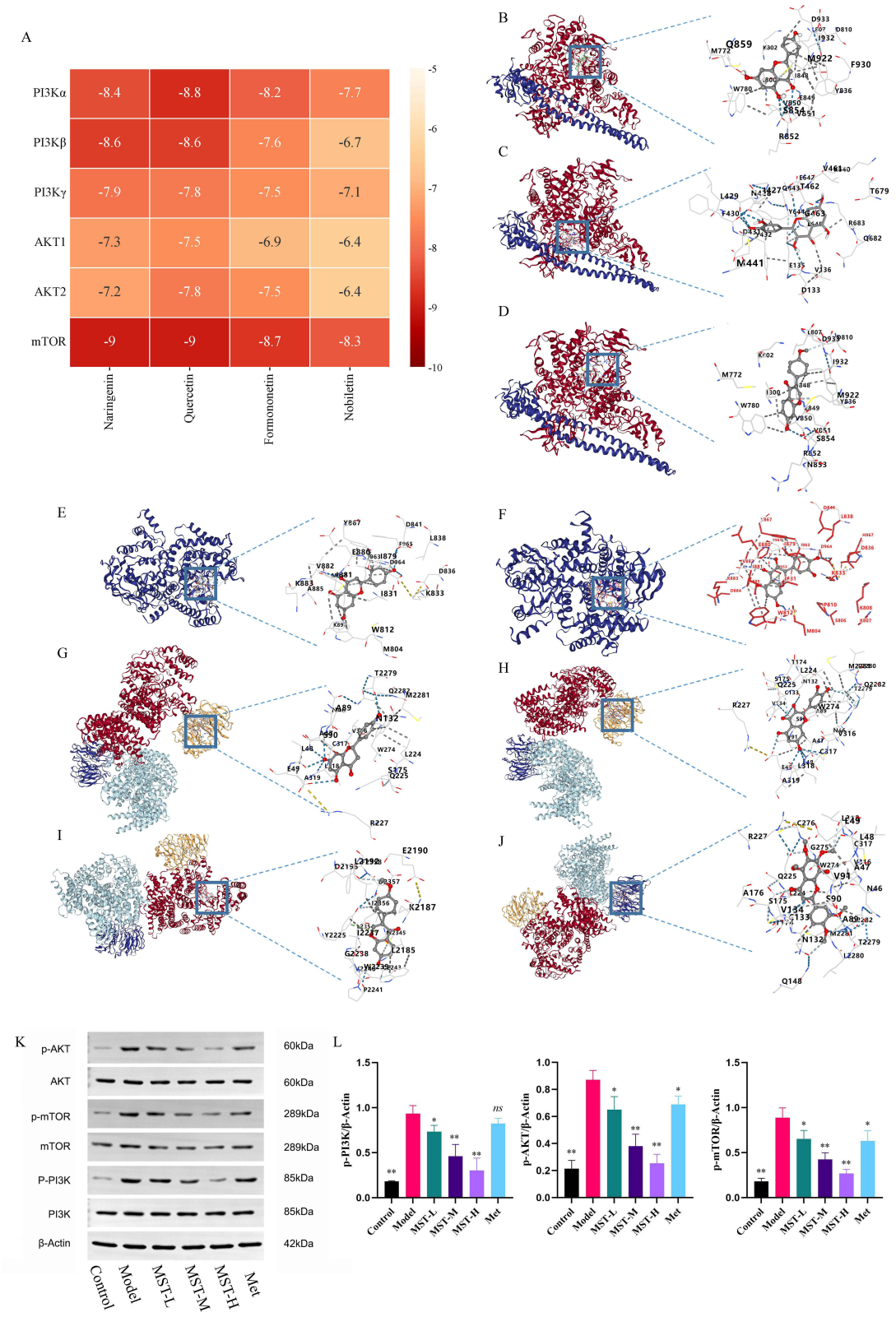

Figure 7 Molecular docking and WB verification. (**A**) Heat map of molecular docking. (**B**) The binding mode of PI3K-α protein with naringenin. (**C**) The binding mode of PI3K-α protein with quercetin. (**D**) The binding mode of PI3K-α protein with formononetin. (**E**) The binding mode of PI3K-β protein with naringenin. (**F**) The binding mode of PI3K-β protein with quercetin. (**G**) The binding mode of mTOR protein with naringenin. (**H**) The binding mode of mTOR protein with quercetin. (**I**) The binding mode of mTOR protein with formononetin. (**J**) The binding mode of mTOR protein with nobiletin. (**K**) Protein expressions of p-PI3K, p-Akt, p-mTOR, PI3K, Akt, and mTOR obtained via Western blot. (**L**) Quantitative analysis of the blot intensities of p-PI3K, p-Akt, and p-mTOR, n = 5. The results are expressed as mean ± SD values. Compared to the Model group, *$p < 0.05$, **$p < 0.01$, *ns*: not significant.

https://doi.org/10.2147/DDDT.S478072 DovePress

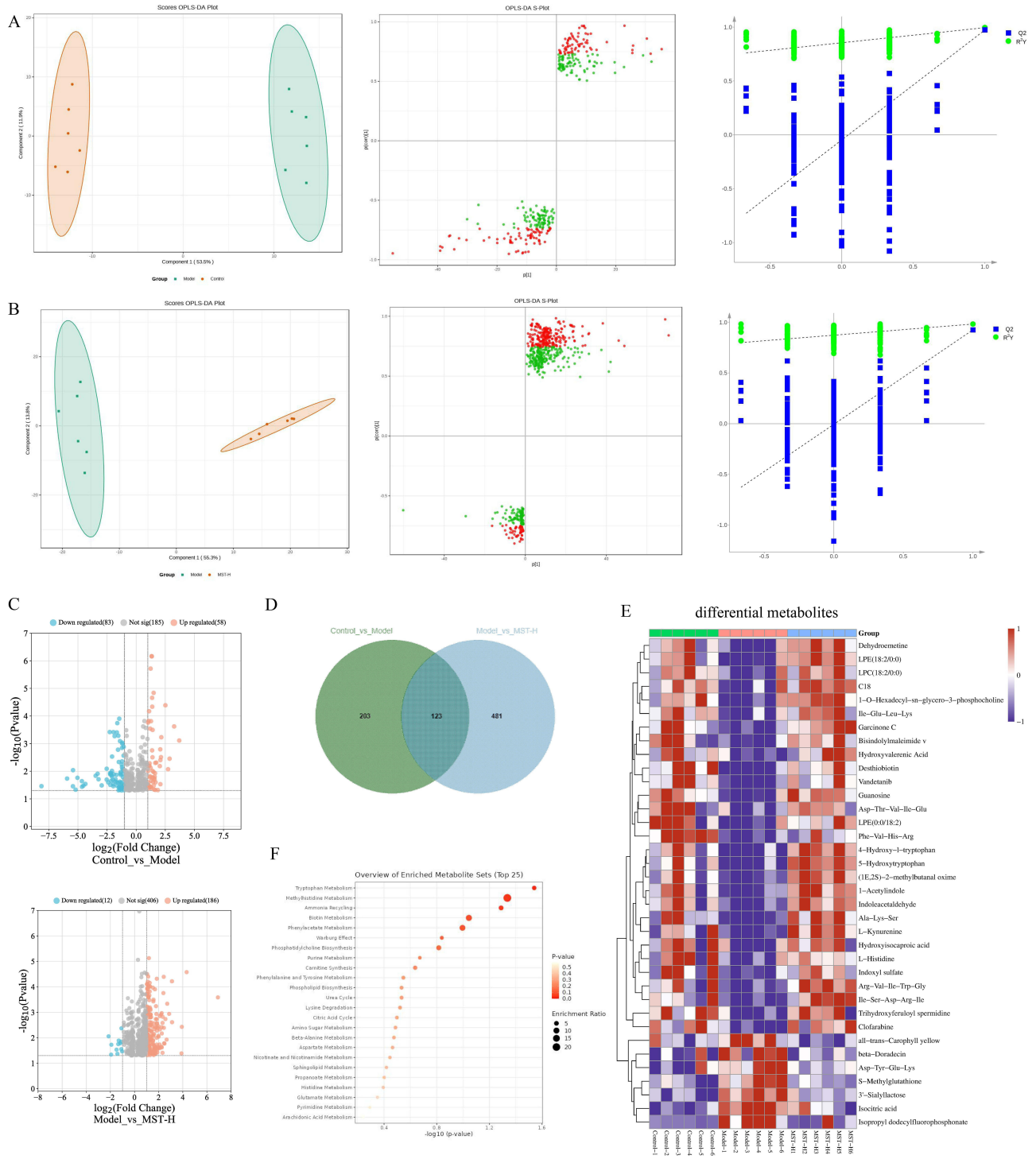

Figure 8 Metabolomic analysis of the MST intervention in MAFLD mice. (**A**) OPLS-DA score diagrams of the Control and Model samples. (**B**) OPLS-DA score diagrams of the Model and MST-H samples. (**C**) Volcano map of differential metabolites in Control vs Model and Model vs MST-H groups. (**D**) Venn diagram of every differential metabolite in Control vs Model and Model vs MST-H groups. (**E**) Heat map of differential metabolites. (**F**) Top 25 enriched KEGG term pathways for differential metabolites (Model vs MST-H), n = 6 per group.

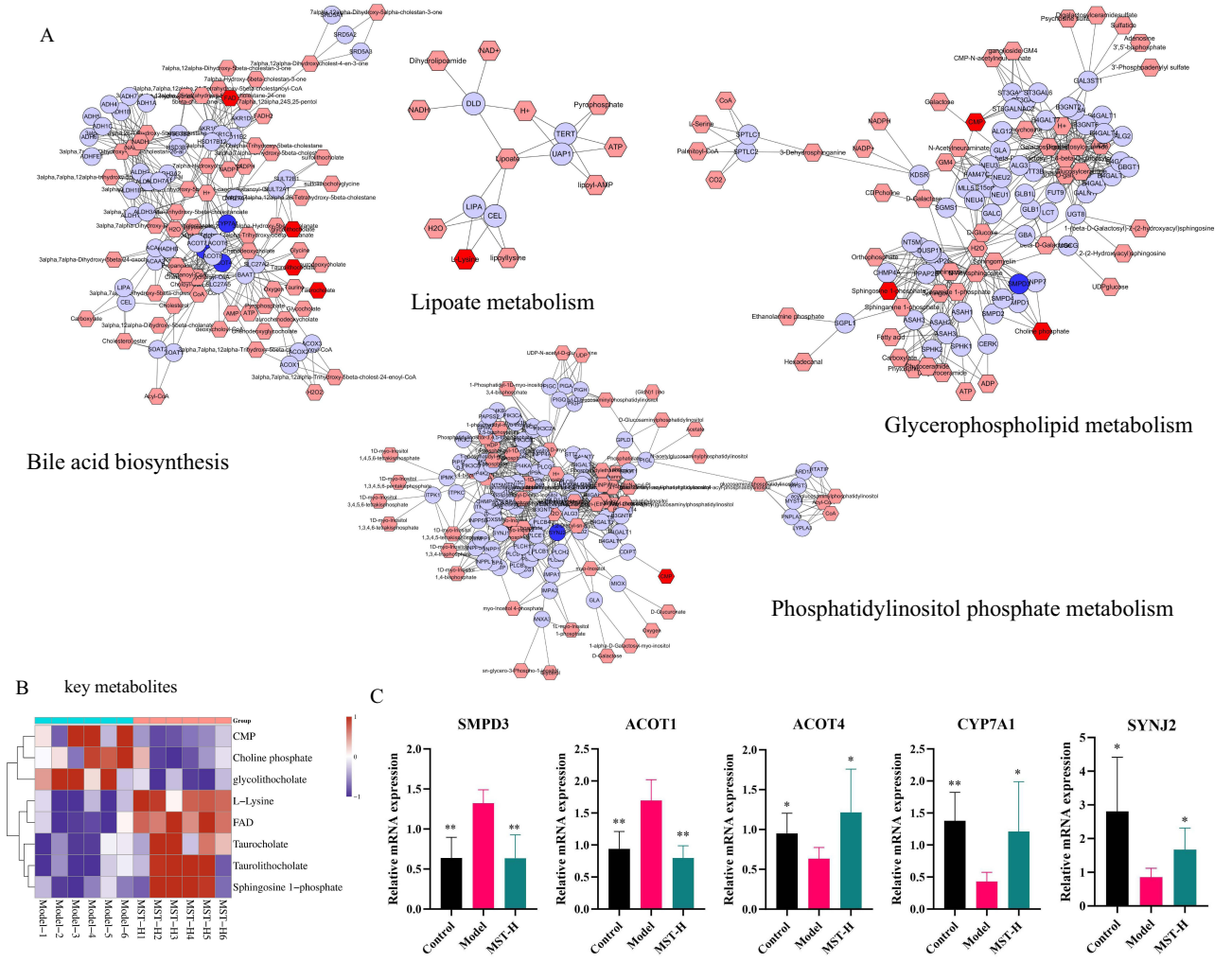

Figure 9 Integrated analysis of transcriptomic and metabolomic data. (**A**) Compound-gene networks for key metabolites and genes, with red hexagons representing active components and blue circles representing key genes. (**B**) Heat map of key metabolites. (**C**) Detection of SMPD3, ACOT1, ACOT4, CYP7A1, and SYNJ2 mRNA expression, n = 6. The results are expressed as mean ± SD values. Compared to the Model group, *$p < 0.05$, **$p < 0.01$.

Discussion

In this study, MAFLD mouse models were created using a HFD, and the effects of MST on MAFLD were assessed through serum lipid profile, IR, body weight, and liver pathology evaluations. The findings showed that MST significantly reduced liver lipid buildup, inflammation, and oxidative stress in the mouse models. Network pharmacology and transcriptomic analyses were conducted to delve into the mechanisms by which MST might improve MAFLD conditions, and the results pointed to autophagy induced by the PI3K/AKT/mTOR signaling pathway. This was further confirmed through various methods, namely ELISA, RT-qPCR, WB, IHC, molecular docking, and metabolomics.

MAFLD is characterized by the pathological accumulation of triglycerides and other lipids in hepatocytes through lipid uptake and excretion, fat synthesis, and fatty acid oxidation.[3] SREBP-1c is a transcription factor for de novo lipogenesis in the liver; it promotes the expression of acetyl-coa carboxylase (ACC) and fatty acid synthetase (FASN), thereby increasing fatty acid synthesis.[18] The cholesterol biosynthesis key enzyme HMGCR catalyzes the conversion of acetyl coenzyme A (acetyl-coa) to mevalonic acid (MVA), thus promoting cholesterol synthesis.[19] FABP4 is a lipid chaperone protein that regulates lipid metabolism by enhancing fatty acid uptake.[20] Cidec promotes lipid droplet growth and reduces fatty acid oxidation by mediating the exchange and transfer of lipids at the binding sites of lipid droplets.[21] In this study, 23 components of MST were identified via UHPLC-Q-Orbitrap-MS/MS. Previous studies have demonstrated that chlorogenic acid,[22] caffeic acid,[23] naringin,[24,25] and quercetin[26] exhibit hepatoprotective effects against HFD-

induced hepatic steatosis by modulating gut microbiota, antioxidant properties, and anti-inflammatory mechanisms. In addition, rutin,[27] limonin,[28] and genistein[29] have been shown to ameliorate MAFLD by boosting lipid metabolism. Mitigating inflammation is one of the key benefits of naringin. Specifically, it counteracts HFD-induced liver lipid deposition by curbing fatty acid intake, reducing de novo fat synthesis, enhancing fatty acid oxidation, and averting gut microbiota imbalance.[30,31] Formononetin enhances liver steatosis by promoting lysosomal biogenesis and lipid autophagy through transcription factor EB mediation.[32] In line with these findings, the present study revealed that MST administration resulted in reduced body weight and decreased levels of TG and LDL-C in MAFLD mice. Moreover, MST attenuated liver lipid accumulation and downregulated the expression of genes associated with liver lipid synthesis, including SREBP-1c, HMGCR, Fabp4, and Cidec.[21,33]

Oxidative stress (OS) refers to an imbalance of oxidation and antioxidation in the body, resulting in a large amount of reactive oxygen species (ROS). This is an important pathogenesis of MAFLD.[34] Increased TG and FFA in the liver can induce lipotoxicity and excessive ROS, leading to OS and, in turn, affecting liver lipid metabolism, reducing fatty acid oxidation, inducing chronic endoplasmic reticulum stress, producing inflammatory cytokines, and damaging mitochondrial function, liver structure, and liver function. It thus promotes the inflammation of liver tissue cells and the progression of MAFLD.[35] At the same time, ROS can reduce SOD and GSH-Px, increase MDA, and aggravate OS.[36] Kupffer cells, which are macrophages in the liver, trigger nonalcoholic steatohepatitis (NASH) by releasing proinflammatory mediators such as TNF-α and CCL2.[37] Free fatty acid (FFA)-induced mitochondrial DNA release triggers NLRP3 inflammasome activation in Kupffer cells, leading to the secretion of the proinflammatory interleukin IL-1β and the progression of MAFLD.[38] Cxcl14, Ccr2, and Cx3cr1 are all chemokines. CXCL14 and Ccr2 regulate the migration and activation of immune cells, promote the release of inflammatory mediators, and aggravate liver injury and steatosis.[39,40] CX3CL1, which is secreted by hepatic stellate cells, binds to its receptor CX3CR1 on Kupffer cells and activates CaMKIIδ, leading to the transfer of HDAC4 from the nucleus to the cytosol and thus the upregulation of Rubicon, in turn inhibiting KC autophagy and exacerbating the chronic intermittent hypoxia-induced apoptosis of Kupffer cells. These factors lead to MAFLD progression.[41] In the present study, MST demonstrated efficacy in reducing the expression of inflammatory factors TNF-α and IL-1β in the serum and liver tissues of the MAFLD mouse models. Furthermore, MST administration led to decreased mRNA expression of liver inflammatory factors TNF-α, IL-1β, Cxcl14, Ccr2, and Cx3cr1. Additionally, MST upregulated the levels of the antioxidant enzymes SOD and GSH-Px in the liver and simultaneously downregulated MDA levels.

Network pharmacology and transcriptomic analysis revealed notable enrichment in both the autophagy and PI3K/AKT pathways, suggesting a correlation between MST's efficacy in improving MAFLD conditions and PI3K/AKT-mediated autophagy. Autophagy functions as a lysosomal degradation pathway and plays a pivotal role in eliminating damaged organelles and misfolded proteins post cell injury induced by endoplasmic reticulum stress or nutrient deprivation. This process ultimately impedes apoptosis and fosters cell viability.[42] During autophagy, LC3-I is covalently bound to phosphatidylethanolamine in the presence of Atg7 and Atg3; LC3-I is lipidated to LC3-II, which binds to the autophagosome membrane; and p62 links the ubiquitinated protein to LC3 and transfers it to the autophagosome.[43] Beclin-1 participates in autophagosome formation by interacting with other proteins, such as VPS34 and ATG14, thereby activating autophagy.[44] The outcomes of this study revealed that MST administration led to reduced LC3-I and p62 protein levels and elevated Beclin-1 and LC3-II protein expression in the liver. These findings suggest that MST alleviates hepatic steatosis through augmentation of the autophagy pathway.

The PI3K/AKT/mTOR signaling pathway plays an important role in the occurrence and development of MAFLD. After insulin binds to insulin receptors, it increases the gene expression of key enzymes of fat synthesis, such as ACC1, FASN, ELOVL6, and SCD1, by activating PI3K, AKT1, and mTORC1.[45] In addition, the PI3K/AKT/mTOR pathway, a classic autophagy pathway, can be activated by multiple receptors (including TLR4), and inhibiting the PI3K/Akt signaling pathway can reduce liver cell damage and lipid disorders.[46] As mTOR is a downstream target of PI3K/Akt, reducing its expression can inhibit autophagy initiation, autophagosome nucleation, phosphorylation, lysosomal biogenesis, and TFEB—a key regulator of autophagy gene expression—as well as increase hepatocyte autophagy to reduce liver lipid deposition.[17] In the present study, MST downregulated the expression of p-PI3K, p-Akt, and p-mTOR proteins in the liver tissues of MAFLD mice, activated autophagy, and improved liver lipid deposition. Studies have shown that

Spp1 can activate the PI3K-AKT signaling pathway, regulate CYP7A1 levels and hepatic acetyl-coa metabolism, disrupt hepatic phosphatidylcholine and cholesterol metabolism, and thus lead to MAFLD progression.[47] COL1A1 and COL1A2 are downstream effector genes of PI3K/AKT and fibrosis-related genes, and they promote the formation of collagen fibers.[48] In sum, MST may activate autophagy by inhibiting the phosphorylation of PI3K/Akt/mTOR signaling pathway and inhibiting the expression of the pathway-related genes Spp1, COL1A1, and COL1A2, thereby improving liver lipid deposition and reducing the expression of fibrosis-related genes.

A variety of metabolites can affect the occurrence and development of MAFLD, among which Hydroxyisocaproic acid is a dietary phenolic acid that helps to alleviate non-alcoholic fatty liver disease (NAFLD) by improving intestinal flora and metabolic function.[49] In addition, Metabolic disturbances constitute the initial event of MAFLD, with tryptophan metabolism emerging as a pivotal factor in MAFLD onset and progression. This essential amino acid pathway holds significant sway over diverse physiological processes, including immune modulation, fibrosis regulation, glucose regulation, lipid metabolism, and hormonal balance. Studies have shown that when tryptophan metabolism is disturbed, the activity of its metabolite cyanuric acid increases, intensifying the inflammatory response and promoting the progression of MAFLD.[50] The metabolomic analysis in the present study showed that MST improved liver lipid deposition in the MAFLD mice by regulating the Hydroxyisocaproic acid and tryptophan metabolism pathway. An association analysis of different genes and metabolites subsequently revealed five gene targets: SMPD3, ACOT1, ACOT4, CYP7A1, and SYNJ2. Notably, AMPKα was found to upregulate SMPD3 expression, leading to increased intestinal ceramide formation and potentially contributing to NAFLD's progression to NASH.[51] ACOT1 and ACOT4 are acyl-coa thioesterases that catalyze the hydrolysis of acyl-coa to FFAs and coenzyme A, and they play an important role in fatty acid metabolism by regulating the ratio of fatty acyl-coa to FFAs in cells, therefore, overexpression of ACOT1 and ACOT4 can ameliorate hepatic steatosis and protect liver function.[52,53] CYP7A1 is the only rate-limiting enzyme in the classic bile acid pathway. Studies have shown that the CYP7A1-AKT-mTOR signaling axis selectively induces autophagy in the livers of mice fed a Western diet, improving hepatocyte integrity and metabolic homeostasis and reducing liver cholesterol.[54] SYNJ2, which belongs to the family of inositol polyphosphate 5-phosphatases, plays a dual role: it not only modulates Akt signaling but also interacts with mitochondrial outer membrane proteins, such as SYNJ2 and synaptic janin2 binding protein (SYNJ2BP), to stimulate the activation of mitochondrial autophagy.[55] The study outcomes indicate that MST effectively reversed the altered gene expression patterns observed in the livers of the MAFLD mice.

Conclusion

In this study, MST exhibited superior efficacy in ameliorating HFD-induced MAFLD in mice. The findings indicate that the mechanism underlying MST's therapeutic effects might involve the augmentation of autophagy via the inhibition of the PI3K/AKT/mTOR signaling pathway in the liver. This provides a solid foundation for employing MST as a potential treatment for MAFLD. Nonetheless, it is worth noting that this study did not involve inhibitor or agonist experiments targeting the PI3K/AKT/mTOR signaling pathway. Subsequent cell experiments are warranted to further validate the findings.

Abbreviations

MST: Modified Suanmei-Tang; MAFLD: metabolic-associated fatty liver disease; HFD: high-fat diet; RT-qPCR: real time quantitative PCR; IR: insulin resistance; TCM: Traditional Chinese medicine; WB: Western blot; Met: Metformin; CHO: cholesterol; NEFAs: non-esterified fatty acids; INS: insulin; TNF-α: tumor necrosis factor-alpha; IL-1β: interleukin-1 beta; MDA: malondialdehyde; SOD: superoxide dismutase; GSH-Px: glutathione peroxidase; Beclin 1: recombinant human beclin 1 protein; LC3 I: microtubule-associated protein light chain 3 I; LC3II: microtubule-associated protein light chain 3 II; P62: sequestosome 1; H&E: hematoxylin and eosin; MST-H: High-Dose MST; MST-M: Medium-Dose MST; MST-L: Low-Dose MST; TG: triglyceride; LDL-C: low-density lipoprotein cholesterol; HDL-C: high-density lipoprotein cholesterol; ALT: alanine aminotransferase; AST: aspartate aminotransferase; PBS: phosphate buffered solution; FDR: false discovery rate; KEGG: Kyoto Encyclopedia of Genes and Genomes; PCA: principal component analysis; VIP: variable importance in projection; OPLS-DA: orthogonal partial least squares-discriminant analysis; IHC: immunohistochemistry.

Data Sharing Statement

All the data involved in this study are available in this published article.

Funding

This work was supported by the sub-project of the National Natural Science Foundation of China (No. 82374331), Sichuan Provincial Department of Science and Technology 2023 Central Leading Local Projects (No. 2023ZYD0049), the basic research business cost project of Institute of Traditional Chinese Medicine, Sichuan Academy of Chinese Medicine Sciences (No. 2023JDKY0028), the basic research business cost project of Institute of Traditional Chinese Medicine, Sichuan Academy of Chinese Medicine Sciences (No. 24JBKY0029).

Disclosure

The authors report no conflicts of interest in this work.

References

1. Van den Bossche J, LA O, Menon D. Macrophage Immunometabolism: where Are We (Going)? *Trends Immunol*. 2017;38(6):395–406. doi:10.1016/j.it.2017.03.001
2. Buzzetti E, Pinzani M, Tsochatzis EA. The multiple-hit pathogenesis of non-alcoholic fatty liver disease (NAFLD). *Metabolism*. 2016;65(8):1038–1048. doi:10.1016/j.metabol.2015.12.012
3. Loomba R, Friedman SL, Shulman GI. Mechanisms and disease consequences of nonalcoholic fatty liver disease. *Cell*. 2021;184(10):2537–2564. doi:10.1016/j.cell.2021.04.015
4. Qian H, Chao X, Williams J, et al. Autophagy in liver diseases: a review. *Mol Aspects Med*. 2021;82:100973. doi:10.1016/j.mam.2021.100973
5. Ueno T, Komatsu M. Autophagy in the liver: functions in health and disease. *Nat Rev Gastroenterol Hepatol*. 2017;14(3):170–184. doi:10.1038/nrgastro.2016.185
6. Han R, Qiu H, Zhong J, et al. Si Miao Formula attenuates non-alcoholic fatty liver disease by modulating hepatic lipid metabolism and gut microbiota. *Phytomedicine*. 2021;85:153544. doi:10.1016/j.phymed.2021.153544
7. Qiu M, Xiao F, Wang T, et al. Protective effect of Hedansanqi Tiaozhi Tang against non-alcoholic fatty liver disease in vitro and in vivo through activating Nrf2/HO-1 antioxidant signaling pathway. *Phytomedicine*. 2020;67:153140. doi:10.1016/j.phymed.2019.153140
8. Yue Z, Jing Y, Wenbo S, Tongting L. Research Progress on Pharmacological Effects and Clinical Application of Wumei(Mume Fructus). *J Liaoning Univ Tradit Chin Med*. 2022;24(07):155–159. doi:10.13194/j.issn.1673-842x.2022.07.034
9. Jian X, Wanxiang Z, Xiaodong W, et al. Research Progress on Chemical Constituents and Pharmacological Effects of Tangerine Peel. *Chinese Wild Plant Resources*. 2022;41(10):72–76+106.
10. Ruiqiang X, Changfu W. Research Progress on Chemical Constituents and Pharmacological Effects of Prepared Glycyrrhiza. *Inf Tradit Chin Med*. 2023;40(04):84–89. doi:10.19656/j.cnki.1002-2406.20230414
11. Ye XL, Huang WW, Chen Z, et al. Synergetic effect and structure-activity relationship of 3-hydroxy-3-methylglutaryl coenzyme A reductase inhibitors from Crataegus pinnatifida Bge. *J Agric Food Chem*. 2010;58(5):3132–3138. doi:10.1021/jf903337f
12. Ye Q, Liu Y, Zhang G, et al. Deficiency of gluconeogenic enzyme PCK1 promotes metabolic-associated fatty liver disease through PI3K/AKT/PDGF axis activation in male mice. *Nat Commun*. 2023;14(1):1402. doi:10.1038/s41467-023-37142-3
13. Chen S, Zhou Y, Chen Y, Gu J. fastp: an ultra-fast all-in-one FASTQ preprocessor. *Bioinformatics*. 2018;34(17):i884–i890. doi:10.1093/bioinformatics/bty560
14. Kim D, Paggi JM, Park C, Bennett C, Salzberg SL. Graph-based genome alignment and genotyping with HISAT2 and HISAT-genotype. *Nat Biotechnol*. 2019;37(8):907–915. doi:10.1038/s41587-019-0201-4
15. National Health Commission of China. Ethical Review Measures for Life Science and Medical Research Involving Humans. [EB/OL] (2023-2-18) [2023-10-16]. Availabe from: https://www.gov.cn/zhengce/zhengceku/2023-02/28/content_5743658.htm. Accessed November 5, 2024.
16. Liu Y, Yang X, Gan J, Chen S, Xiao ZX, Cao Y. CB-Dock2: improved protein-ligand blind docking by integrating cavity detection, docking and homologous template fitting. *Nucleic Acids Res*. 2022;50(W1):W159–w164. doi:10.1093/nar/gkac394
17. Liu B, Deng X, Jiang Q, et al. Scoparone improves hepatic inflammation and autophagy in mice with nonalcoholic steatohepatitis by regulating the ROS/P38/Nrf2 axis and PI3K/AKT/mTOR pathway in macrophages. *Biomed Pharmacother*. 2020;125:109895. doi:10.1016/j.biopha.2020.109895
18. Xia M, Chandrasekaran P, Rong S, Fu X, Mitsche MA. Hepatic deletion of Mboat7 (LPIAT1) causes activation of SREBP-1c and fatty liver. *J Lipid Res*. 2021;62:100031. doi:10.1194/jlr.RA120000856
19. Kerr TA, Davidson NO. Cholesterol and nonalcoholic fatty liver disease: renewed focus on an old villain. *Hepatology*. 2012;56(5):1995–1998. doi:10.1002/hep.26088
20. Wei D, Wu S, Liu J, et al. Theobromine ameliorates nonalcoholic fatty liver disease by regulating hepatic lipid metabolism via mTOR signaling pathway in vivo and in vitro. *Can J Physiol Pharmacol*. 2021;99(8):775–785. doi:10.1139/cjpp-2020-0259
21. Xia QS, Gao Y, Wen-Bin W, et al. Ban-xia-xie-xin-tang ameliorates hepatic steatosis by regulating Cidea and Cidec expression in HFD-fed mice. *Phytomedicine*. 2022;105:154351. doi:10.1016/j.phymed.2022.154351
22. Shi A, Li T, Zheng Y, et al. Chlorogenic Acid Improves NAFLD by Regulating gut Microbiota and GLP-1. *Front Pharmacol*. 2021;12:693048. doi:10.3389/fphar.2021.693048
23. Mu HN, Zhou Q, Yang RY, et al. Caffeic acid prevents non-alcoholic fatty liver disease induced by a high-fat diet through gut microbiota modulation in mice. *Food Res Int*. 2021;143:110240. doi:10.1016/j.foodres.2021.110240

24. Li X, Yao Y, Wang Y, et al. Effect of Hesperidin Supplementation on Liver Metabolomics and Gut Microbiota in a High-Fat Diet-Induced NAFLD Mice Model. *J Agric Food Chem*. 70(36):11224–11235. doi:10.1021/acs.jafc.2c02334
25. Xie Q, Gao S, Lei M, Li Z. Hesperidin suppresses ERS-induced inflammation in the pathogenesis of non-alcoholic fatty liver disease. *Aging (Albany NY)*. 2022;14(3):1265–1279. doi:10.18632/aging.203817
26. Chen L, Liu J, Mei G, et al. Quercetin and non-alcoholic fatty liver disease: a review based on experimental data and bioinformatic analysis. *Food Chem Toxicol*. 2021;154:112314. doi:10.1016/j.fct.2021.112314
27. El-Shial EM, Kabbash A, El-Aasr M, El-Feky OA, El-Sherbeni SA. Elucidation of Natural Components of Gardenia thunbergia Thunb. Leaves: effect of Methanol Extract and Rutin on Non-Alcoholic Fatty Liver Disease. *Molecules*. 2023;28(2):879. doi:10.3390/molecules28020879
28. Li Y, Yang M, Lin H, et al. Limonin Alleviates Non-alcoholic Fatty Liver Disease by Reducing Lipid Accumulation, Suppressing Inflammation and Oxidative Stress. *Front Pharmacol*. 2021;12:801730. doi:10.3389/fphar.2021.801730
29. Xin X, Chen C, Hu YY, Feng Q. Protective effect of genistein on nonalcoholic fatty liver disease (NAFLD). *Biomed Pharmacother*. 2019;117:109047. doi:10.1016/j.biopha.2019.109047
30. Mu H, Zhou Q, Yang R, et al. Naringin Attenuates High Fat Diet Induced Non-alcoholic Fatty Liver Disease and Gut Bacterial Dysbiosis in Mice. *Front Microbiol*. 2020;11:585066. doi:10.3389/fmicb.2020.585066
31. Zhang X, Zhang Y, Gao W, et al. Naringin improves lipid metabolism in a tissue-engineered liver model of NAFLD and the underlying mechanisms. *Life Sci*. 277:119487. doi:10.1016/j.lfs.2021.119487
32. Wang Y, Zhao H, Li X, et al. Formononetin alleviates hepatic steatosis by facilitating TFEB-mediated lysosome biogenesis and lipophagy. *J Nutr Biochem*. 2019;73:108214. doi:10.1016/j.jnutbio.2019.07.005
33. Méndez-Giménez L, Rodríguez A, Balaguer I, Frühbeck G. Role of aquaglyceroporins and caveolins in energy and metabolic homeostasis. *Mol Cell Endocrinol*. 2014;397(1–2):78–92. doi:10.1016/j.mce.2014.06.017
34. Katsiki N, Mikhailidis DP, Mantzoros CS. Non-alcoholic fatty liver disease and dyslipidemia: an update. *Metabolism*. 2016;65(8):1109–1123. doi:10.1016/j.metabol.2016.05.003
35. Clare K, Dillon JF, Brennan PN. Reactive Oxygen Species and Oxidative Stress in the Pathogenesis of MAFLD. *J Clin Transl Hepatol*. 10(5):939–946. doi:10.14218/jcth.2022.00067
36. Liu Y, Xu W, Zhai T, You J, Chen Y. Silibinin ameliorates hepatic lipid accumulation and oxidative stress in mice with non-alcoholic steatohepatitis by regulating CFLAR-JNK pathway. *Acta Pharm Sin B*. 2019;9(4):745–757. doi:10.1016/j.apsb.2019.02.006
37. Tosello-Trampont AC, Landes SG, Nguyen V, Novobrantseva TI, Hahn YS. Kuppfer cells trigger nonalcoholic steatohepatitis development in diet-induced mouse model through tumor necrosis factor-α production. *J Biol Chem*. 2012;287(48):40161–40172. doi:10.1074/jbc.M112.417014
38. Pan J, Ou Z, Cai C, et al. Fatty acid activates NLRP3 inflammasomes in mouse Kupffer cells through mitochondrial DNA release. *Cell Immunol*. 2018;332:111–120. doi:10.1016/j.cellimm.2018.08.006
39. Matsushita Y, Hasegawa Y, Takebe N, et al. Serum C-X-C motif chemokine ligand 14 levels are associated with serum C-peptide and fatty liver index in type 2 diabetes mellitus patients. *J Diabetes Investig*. 2021;12(6):1042–1049. doi:10.1111/jdi.13438
40. Liu B, Xiang L, Ji J, et al. Sparcl1 promotes nonalcoholic steatohepatitis progression in mice through upregulation of CCL2. *J Clin Invest*. 2021;131(20). doi:10.1172/jci144801
41. Li Y, Chen Y, Xiao X, Deng S, Kuang J, Wang Y. CX3CL1 represses autophagy via CX3CR1/ CaMKIIδ/HDAC4/Rubicon axis and exacerbates chronic intermittent hypoxia induced Kupffer cell apoptosis. *Cell Signal*. 2023;111:110873. doi:10.1016/j.cellsig.2023.110873
42. Chen CL, Lin YC. Autophagy Dysregulation in Metabolic Associated Fatty Liver Disease: a New Therapeutic Target. *Int J Mol Sci*. 2022;23(17):10055. doi:10.3390/ijms231710055
43. Ren Q, Sun Q, Fu J. Dysfunction of autophagy in high-fat diet-induced non-alcoholic fatty liver disease. *Autophagy*. 2024;20(2):221–241. doi:10.1080/15548627.2023.2254191
44. Zhang R, Yang Y, He C, et al. RUNDC1 inhibits autolysosome formation and survival of zebrafish via clasping ATG14-STX17-SNAP29 complex. *Cell Death Differ*. 2023;30(10):2231–2248. doi:10.1038/s41418-023-01215-z
45. Hinds TD Jr, Creeden JF, Gordon DM, Stec DF, Donald MC, Stec DE. Bilirubin Nanoparticles Reduce Diet-Induced Hepatic Steatosis, Improve Fat Utilization, and Increase Plasma β-Hydroxybutyrate. *Front Pharmacol*. 2020;11:594574. doi:10.3389/fphar.2020.594574
46. Cheng C, Liu XH, He J, et al. Apolipoprotein A4 Restricts Diet-Induced Hepatic Steatosis via SREBF1-Mediated Lipogenesis and Enhances IRS-PI3K-Akt Signaling. *Mol Nutr Food Res*. 2022;66(18):e2101034. doi:10.1002/mnfr.202101034
47. Nuñez-Garcia M, Gomez-Santos B, Buqué X, et al. Osteopontin regulates the cross-talk between phosphatidylcholine and cholesterol metabolism in mouse liver. *J Lipid Res*. 2017;58(9):1903–1915. doi:10.1194/jlr.M078980
48. Blackstock CD, Higashi Y, Sukhanov S, et al. Insulin-like growth factor-1 increases synthesis of collagen type I via induction of the mRNA-binding protein LARP6 expression and binding to the 5' stem-loop of COL1a1 and COL1a2 mRNA. *J Biol Chem*. 2014;289(11):7264–7274. doi:10.1074/jbc.M113.518951
49. Ji L, Deng H, Xue H, et al. Research progress regarding the effect and mechanism of dietary phenolic acids for improving nonalcoholic fatty liver disease via gut microbiota. *Compr Rev Food Sci Food Saf*. 2023;22(2):1128–1147. doi:10.1111/1541-4337.13106
50. Teunis C, Nieuwdorp M, Hanssen N. Interactions between Tryptophan Metabolism, the Gut Microbiome and the Immune System as Potential Drivers of Non-Alcoholic Fatty Liver Disease (NAFLD) and Metabolic Diseases. *Metabolites*. 12(6):514. doi:10.3390/metabo12060514
51. Chen B, Sun L, Zeng G, et al. Gut bacteria alleviate smoking-related NASH by degrading gut nicotine. *Nature*. 2022:610(7932):562–568. doi:10.1038/s41586-022-05299-4
52. Zhong D, Cai J, Hu C, et al. Inhibition of mPGES-2 ameliorates NASH by activating NR1D1 via heme. *Hepatology*. 78(2):547–561. doi:10.1002/hep.32671
53. Heden TD, Franklin MP, Dailey C, Mashek MT, Chen C, Mashek DG. ACOT1 deficiency attenuates high-fat diet-induced fat mass gain by increasing energy expenditure. *JCI Insight*. 8(18):e160987. doi:10.1172/jci.insight.160987
54. Wang Y, Ding Y, Li J, et al. Targeting the Enterohepatic Bile Acid Signaling Induces Hepatic Autophagy via a CYP7A1-AKT-mTOR Axis in Mice. *Cell Mol Gastroenterol Hepatol*. 2017;3(2):245–260. doi:10.1016/j.jcmgh.2016.10.002
55. Harbauer AB, Hees JT, Wanderoy S, et al. Neuronal mitochondria transport Pink1 mRNA via synaptojanin 2 to support local mitophagy. *Neuron*. 110(9):1516–1531.e9. doi:10.1016/j.neuron.2022.01.035